SOCIETÀ TOSCANA DI Scienze Naturali

RESIDENTE IN PISA

ATTI DELLA SOCIETÀ TOSCANA DI SCIENZE NATURALI

MEMORIE • SERIE A • VOLUME CXXIX • ANNO 2022

Edizioni ETS

Atti Soc. Tosc. Sci. Nat., Mem., Serie A, 129 (2022)
pagg. 27-41; figg. 22; tabb. 4; *doi: 10.2424/ASTSN.M.2022.04*

Vincenzo De Luca [(1)], Marco Lezzerini [(2)], Francesco Cavalcante [(3)], Cosimo Marano [(4)], Giuseppe Palladino [(5,6)], Mario Bentivenga [(1)]

A LARGE STRAIN FINITE ELEMENT METHOD MODEL OF SANDSTONE MATERIAL IN MASONRY BUILDING

Abstract - V. De Luca, M. Lezzerini, F. Cavalcante, C. Marano, G. Palladino, M. Bentivenga, *A large strain Finite Element Method model of sandstone material in masonry building.*

The use of squared natural stones in traditional constructions is quite common in many Italian regions. Natural stones are basic materials of traditional masonries. The characterization of a natural stone, as basic material of masonry, is an important task in building design and rehabilitation. An appropriate knowledge of the stone mechanical behavior is fundamental for the analyses with the Finite Element Method, frequently adopted to design and check static and dynamic safety of both new and existing buildings. Accordingly to this, in the present paper we have analyzed the natural sandstone material by means of a Finite Element Method model, based on a large strain formulation, to characterize the mechanical stress-strain path, from elastic to plastic and damage until failure, of the investigated sandstone. Specimens of sandstone are experimental tested under uniaxial compression and displacement control. The numerical results are matched up to the analogous experimental measurements in order to verify the accuracy of the present model. On the basis of the obtained findings, the model has demonstrated to be a consistent tool for checking the existing masonry buildings; it allows a consistent representation of a quasi-brittle material.

Key words - Finite Element Method, elastoplastic damage coupled, anisotropic multi-yield plasticity, finite strains, natural stone constitutive law, masonry building

Riassunto - V. De Luca, M. Lezzerini, F. Cavalcante, C. Marano, G. Palladino, M. Bentivenga, *Un modello basato sul Metodo ad Elementi Finiti a larga deformazione della pietra arenaria in costruzioni in muratura.*

L'uso delle pietre naturali squadrate nelle costruzioni tradizionali è abbastanza comune in molte regioni italiane. Le pietre naturali sono materiali base delle murature tradizionali. La caratterizzazione di una pietra naturale, come materiale di base della muratura, è un aspetto importante nella progettazione e riabilitazione edilizia. Un'adeguata conoscenza del comportamento meccanico della pietra è fondamentale per le analisi con il Metodo degli Elementi Finiti, frequentemente adottato per progettare e verificare la sicurezza statica e dinamica di edifici sia nuovi che esistenti. Nell'ambito del suddetto tema, nel presente lavoro abbiamo analizzato il materiale arenaria naturale per mezzo di un modello a Metodo ad Elementi Finiti, basato su una formulazione di grande deformazione, per caratterizzare il percorso meccanico tensione-deformazione, da elastico a plastico e danneggiamento fino a rottura, dell'arenaria studiata. I provini di arenaria sono testati sperimentalmente a compressione uniassiale sotto controllo di spostamento. I risultati numerici sono confrontati con le corrispondenti misure sperimentali al fine di verificare l'accuratezza del presente modello. Sulla base delle risultanze ottenute, il modello si è dimostrato uno strumento coerente per la verifica degli edifici in muratura esistenti; esso permette una rappresentazione appropriata di un materiale quasi fragile.

Parole chiave - Metodo ad Elementi Finiti, elastoplasticità combinata con danneggiamento, plasticità anisotropa multi-soglia, grandi deformazioni, legge costitutiva pietra naturale, costruzione di muratura

Introduction

Currently, the restoration and conservation of historical buildings, both civil and rural, is a topic of certain significance among scientific literature (Triantafillou & Fardis, 1997; Binda *et al.*, 1997; Lourenço, 2006; Sandbhor & Botre, 2013; Varas-Muriel *et al.*, 2015; Betti *et al.*, 2016; Vasanelli *et al.*, 2016; Mosele *et al.*, 2016; Guerreiro *et al.*, 2017; Yavartanoo & Kang, 2022). Many historical buildings often require strengthening interventions to restore or to reinstate their structure and their aged materials. Structural and material deficiencies or requirements for earthquake-safe can require specific interventions (Lucibello *et al.*, 2013; Brandonisio *et al.*, 2013) by respecting the original architecture, structure and materials (Ramos & Lourenço, 2004).

Generally, historic constructions of masonry are made using stone blocks joined by a mortar stratum. Natural stones, widely assorted, have been the most durable and prevailing basic material in constructions until today (Pereira & Marker, 2016; Šekularac *et al.*, 2019; Kaur *et al.*, 2021). Masonry is an irregular composite structure whose two distinct resistant components, stone blocks and mortar, solidly support loads through compression distribution. Masonry exerts a strength,

(1) Dipartimento di Scienze, Università della Basilicata, viale Ateneo Lucano 10 - 85100 Potenza, Italy
(2) Dipartimento di Scienze della Terra, Università di Pisa, via S. Maria 53 - 56126 Pisa, Italy
(3) IMAA, CNR, Contrada Santa Loja s.n.c. Tito Scalo - 85050 Potenza, Italy
(4) SAFE, Università della Basilicata, viale Ateneo Lucano 10 - 85100 Potenza, Italy
(5) Italconsult S.p.a., via di Villa Ricotti 20 - 00161 Rome, Italy
(6) Department of Geology and Geophysics, University of Aberdeen - Aberdeen, UK
Corresponding author: Vincenzo De Luca (vincenzo.deluca@unibas.it)

which is high in compression and low in tension and shear. Normally, in a masonry structure failure is a consequence of fractures in mortar components. These fractures progressively grow parallel to the direction of loading (García, *et al.*, 2012). This can be attributed to the fact that, in historic masonries, mortar often holds a really weak stress.

The mechanical behavior and strength evaluation of the natural stone component is a driving key in masonry design for the structural rehabilitation. Additionally, when a Finite Element Method (FEM) code is employed in masonry design, a complete evaluation of masonry behavior and strength must be considered, particularly in a pushover type analysis. This issue is still quite under study in research activity. A good cognition of the mechanical behavior of masonry is based on an accurate knowledge of both masonry basic constituents: stone and mortar. An approach, commonly adopted in many numerical FEM models, is to analyze the mechanical behavior of masonry constructions (Senthivel & Lourenço, 2009) by separately modeling each constituent within the overall composite.

The nonlinear mechanical behavior of stone materials can be attributed to two kinds of inelastic deformations: plastic flow and mainly damage process (Mazars, 1986; Molladavoodi & Mortazavi, 2011). The plastic flow is a process caused by local shear stresses which create extension of existing faults. In a stone, plastic flow arises in the portions where the material is undamaged (Chiarelli *et al.*, 2003), and at a macroscopic level, on the whole, it leaves quite unchanged the material stiffness (Yazdani & Schreyer, 1988; Wu & Faria, 2006). Stone exhibits a behavior, which experiences, in a mechanical sense, damage and failure both under tensile, compressive and shear loading. This behavior can be assimilated to that of quasi-brittle material. The damage is a primary cause of irreversible deformations in quasi-brittle materials, caused by critical enlargement of micro-cracks by generating meso-cracks (Shao *et al.*, 2006).

Stone materials are intrinsically discontinuous in their structure, the stress-strain distributions, varying within the material mass, induced by micro-structural inhomogeneity, take a major part in the brittle fracture of some stones.

In scientific literature, various constitutive models, focused on damage, have been proposed to represent the mechanical behavior of stone materials (Grady & Kipp, 1979; Krajcinovic & Silva, 1982; Gao *et al.*, 2020; Xie *et al.*, 2022). And, various FEM numerical models, based on an elastic-plastic-damage representation of material constitutive equation (Faria *et al.*, 1998; Hatzigeorgiou *et al.*, 2001; Agelopoulou *et al.*, 2005), have been proposed to perform the mechanical behavior of a quasi-brittle material. Also, in scientific literature some analytical and experimental works have been reported specifically addressed to anisotropic elastoplastic-damage behavior of masonry structures, in historical constructions, (Mazars, 1986; Hatzigeorgiou *et al.*, 2001) and other works to analyze an historical or a monumental building by the FEM (Ramalho *et al.*, 2008; Romera *et al.*, 2008a, b; Ivorra *et al.*, 2009).

The use of blocks of sandstone in traditional regional constructions and historic buildings is quite common. An example is the "Gorgoglione Stone" (belongs to the Gorgoglione Formation (Selli, 1962)) which has been used, until today, in masonry construction in Southern Italy, in territorial areas adjacent to the quarries of extraction. Aiming to modeling the constitutive law of that sandstone, the present work focuses to numerically study the mechanical behavior of the stone material, not of the mortar and nor of the masonry assemblage. This study is conducted by employing a FEM framework, with large strain formulation, in conjunction with a material model elastic-plastic coupled with damage, based on a multi-surface yield approach (De Luca, 2022). The proposed FEM model is verified for its correctness by accordingly comparing the numerical results, determined on uniaxial compression tests, with the corresponding experimental tests on sandstone specimens, here reported.

MATERIALS AND METHODS

Theory of the material model

The proposed FEM framework employs a time-dependent constitutive model for damage-coupled elastic-plasticity of an anisotropic material, an approach based on a rate-dependent (de Angelis, 2012a; b; c; d; e) formulation of material inelasticity. A detailed statement of this approach is reported in the work of De Luca (2022), which also is supported by other experimental studies of non-isotropic materials (De Luca & Sabia, 2007; De Luca & Della Chiesa, 2013; De Luca & Marano, 2012) and by a study on geomaterials (De Luca *et al.*, 2015). Here, only a very short description follows.

Starting from the classical continuum mechanics theory, by a large strain formulation, adopting a multiplicative split of the deformation gradient tensor, in an intermediate configuration, the anisotropic constitutive equations are formulated. The invariance principle of tensor variables and the thermodynamic consistence of dissipation are assured accounting for, in material response, the elastic energy and the inelastic dissipated energies, expressed by multi-yield functionals. The evolution laws, kinematically constrained, are devised by applying the maximum dissipation principle to the yield functionals, specific of the investigated material. Here, for the sandstone, non-deviatoric yields are adopted. The continuous evolution equations are approximated into algebraic ones in the context of the FEM framework. Within the general return mapping method, these algebraic equations are integrated by the backward-Euler integration method, implicit in time. The system of governing non-linear equations is numerically solved by using the iterative Newton-Raphson method. The above presented formulation, with related algorithms, is implemented in a software code.

Experimental work

Material and specimens - The selected variety of "Gorgoglione Stone" is a grey sandstone, with rare light brown-colored tones. It is fine-grained, moderately hard, its matrix arrangement includes sand grains and natural cement, chaotically distributed into the bulk mass.

Two sets of sandstone specimens are obtained from a unique sample of rock extracted from a quarry. The specimens are manufactured as follows: a set of 10 specimens in the longitudinal direction (CL) of the geological stratum (Fig. 1a), and 10 specimens in the tangential direction (CT) of the geological stratum (Fig. 1b). The specimens are cut and shaped into cubes with a side of 25 mm. These non-standard specimens are mainly motivated by the need of a reduced impact of destructive tests on the solidity conservation of historical masonries (Indelicato, 1993; Skłodowski, 2006; Tuncan *et al.*, 2008). Accordingly, cylinder micro-cores, with a diameter of 28 mm (Indelicato, 1998; Vasanelli *et al.*, 2016; Vasanelli *et al.*, 2017) or small cubic specimen, with a side of 15÷25 mm, are used to experimental test masonry in historical building (Drdácký *et al.*, 2008; Drdácký & Slížková, 2008; Alejandre et al., 2014). However, in our experiments the specimen's dimensions are large relatively to grain size of the investigated stone.

All the specimens are leveled and flatted by an electromechanical tool and then stored in laboratory for at least 15 days at room temperature and humidity.

Test method and procedure - A Galdabini PMA10 electromechanical testing press, computer-assisted, is employed to carry out the experimental tests. The press is equipped, into its cross-head, with a force transducer, whose maximum capacity is 100 kN, and a linear variable displacement transducer (LVDT), whose maximum displacement is 50 mm. During the uniaxial compression tests (Figs 2 and 3), the measured values by the load transducer and the displacement transducer are data-logged and memorized at a prefixed sampling rate by the digital press machine. The experimental tests are executed under displacement control. Therefore, the bottom cross-head of machine is remained fixed while the upper cross-head is moved at a constant displacement rate of 1 mm/min until rupture. Rupture is automatically detected by the control software of the testing machine, when a major drop in the load-displacement path occurs. All the experimental tests are executed at room temperature and humidity, in the laboratory of the SAFE School, University of Basilicata, Italy.

a)

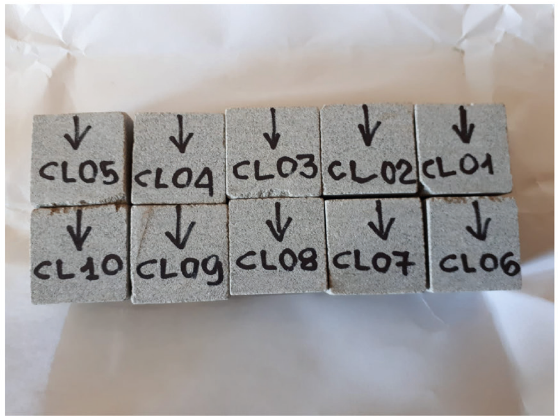

b)

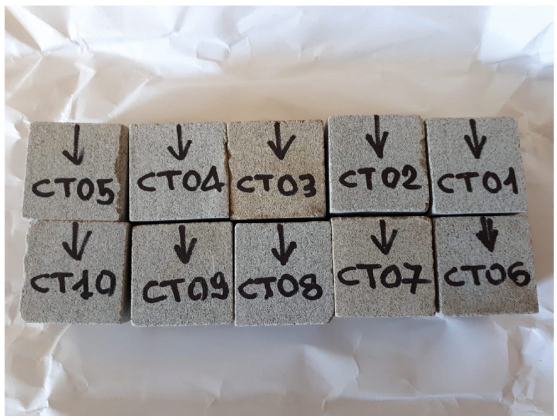

Figure 1. Photos of the sets of specimens of sandstone prepared for the compression test along the longitudinal direction (a) and along the tangential direction (b).

Material parameters determination - A fundamental step of the work is the estimation of mechanical properties of the material to be directly assumed for the model, as input into the numerical runs of the FEM code. Firstly we have carried out the elaboration of the experimental data by means of fitting technique to estimate the mechanical parameters of the material. The material properties are determined as follows: some from the experimental stage, other from analytical relationships, the material density from a previous work (De Luca *et al.*, 2019), and the rest material properties from literature.

Figure 2. Experimental setup of a cubic specimen (CL01) loaded in longitudinal direction.

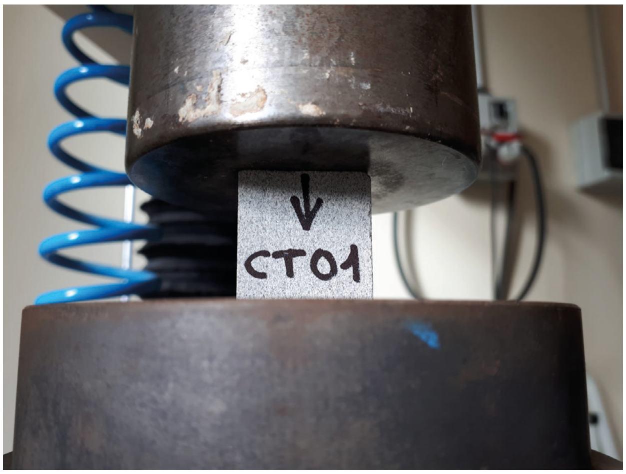

Figure 3. Experimental setup of a cubic specimen (CT01) loaded in tangential direction.

According to the proposed model, nine components are assumed for each tensor representation. These components for the elastic constitutive law are the components of the elastic tensor, and the six Poisson's ratios, which have to respect the relative coherence conditions (Lekhnitskii, 1963; Jones & Ashby, 2018). The elastic moduli are estimated, from the experimental data of uniaxial compression tests, by means of a linear least-square regression with a coefficient up to 0.995. However, the first part, of crack closure process, of the stress-strain curve is included in the elastic range. The Poisson's ratios are assumed from literature (Gercek, 2007).
The other material properties, which enter the FEM code, are nine tensor components for the plastic multi-yield: minimum and maximum stress strengths; minimum and maximum strain strengths; minimum and maximum ultimate strains. The same properties are assumed for the damage multi-yield. No plastic and nor damage hardening is taken into account. Some of these properties are consistently retrieved from the experimental data and others are analytically determined.

Numerical analysis

On the basis of the estimated material parameters the major purpose of the numerical modeling is to perform the numerical prediction of the mechanical behavior of the material, both along the elastic and post-elastic path until rupture. To check the effectiveness of the present model, a comparison of the numerical results against the experimental data is here reported. The numerical results are obtained by referring to the nominal dimensions and the mechanical characteristics of a real specimen in order to effectively reproduce the test on the same conditions.

Numerical model validation

The stress-strain couples of values in an experimental test of a sandstone specimen, under uniaxial compression loading, are considered in the validation stage. Based on the measured values of the displacement, divided by the initial height of the cubic specimen, and of the applied force, divided by the initial cross-section of the cubic specimen, the whole stress-strain measurements diagram of the examined material is traced. Also, along the post-peak path of this diagram the brittleness and failure kind of the material can be identified, inside the overall mechanical behavior.

Mesh, boundary conditions and loading - We have adopted a fully three dimensional representation of the test in the FEM numerical analysis, whose mesh, representing a specimen, is illustrated in Fig. 4. The mesh is constituted by 3375 elements of hexahedral type, with 8 integration points on the vertex, which totalizes 4096 measuring points.
At the points belonging to the bottom face of the mesh, appropriate boundary conditions, of "uniaxial strain" type, which restrain all the degree of freedom, are applied (Fig. 4). In the mesh the lateral sides are left free to move in all the directions.
To reproduce the uniaxial compression loading of the cubic specimen, under displacement control, incremental steps of displacement, represented by a time function variable, are imposed at the points belonging to the top face of the mesh.

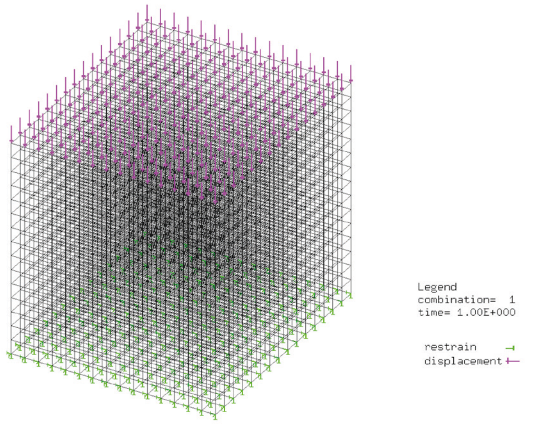

Figure 4. Model mesh of the specimen with the displacement loads and the boundary conditions.

Results and discussion

Experimental results

Here we report and discuss the results obtained in the present experimental work.

We have already measured in a previous work (De Luca *et al.*, 2019) some physical properties of the analyzed sandstone: the real density of the sandstone is 2630 ± 10 kg/m^3 and the apparent density is 2487 ± 6 kg/m^3.

Material parameters determination - The mechanical parameters here estimated, on the basis of the experimental tests, are the values of the longitudinal elastic moduli, relative to the only valid trials. They are reported in Tab. 1 for longitudinal direction of loading (CL) and in Tab. 2 for tangential (CT) direction of loading. Furthermore, the minimum, the maximum and the mean values and the Root Mean Square Error (RMSE) of: elastic modules, compressive strength and corresponding strain, strain at failure are listed in both Tabs 1 and 2.

The estimation of the undamaged elastic modulus is 4383±364 N/mm^2 along the longitudinal direction of loading (Tab. 1), and is 3766±367 N/mm^2 along the tangential direction of loading (Tab. 2).

The measured uniaxial compression strength value on the cubes, loaded in the longitudinal direction, is 135.4±11.8 N/mm^2. The value obtained on cubes loaded in the tangential direction is 130.4±15.1 N/mm^2. The corresponding strain at peak stress is 0.04048±0.00482 mm/mm, and 0.03774±0.00644 mm/mm, for longitudinal direction and tangential direction of loading, respectively. The strain at failure is 0.04507±0.00563 mm/mm and 0.04246±0.00761 mm/mm for longitudinal direction and tangential direction of loading, respectively.

By reading the high RMSE of the stress and of the strain values, reported in Tabs 1 and 2, we can note that the specimens give us an idea about the significant heterogeneity of the material. This aspect can be attributed to the intrinsic nature of stone.

The mechanical properties and the strength properties assumed for sandstone in the numerical runs are reported in Tabs 3 and 4, respectively. In Tab. 4 the tensile strength for the longitudinal direction is established, according to literature findings on brittle rocks (Hudson & Harrison, 1997), as 1/10 of compression strength. The longitudinal direction of loading (CL) corresponds to the material direction of the local axes in Tab. 3 and Tab. 4; obviously when the tangential direction of loading (CT) is considered the above properties, listed in Tab. 3 and Tab. 4, must be properly rotated.

Failure modes - Being a heterogeneous material, the stone is characterized by a quite pronounced variation in its mechanical behavior, in an experimental test, for different specimens even of same material and at identical specimen size and testing settings. This also is a direct consequence of the heterogeneity in the coalescence development. However, to estimate the mechanical parameters of the material, at a macroscopic point of view, the influence of heterogeneity on material behavior and strength can be averaged. Yet heterogeneity influences the complete path of stress-strain, chiefly the post-peak softening and brittleness. In fact, as well known in scientific literature for quasi-brittle materials, along most part of loading increment, the specimen is subjected to inner micro-structural adjustments. Due to these fabric adjustments the vanishing of cohesion in stone matrix increases the material damage and decreases the elastic modulus. These effects initially seem not influencing the mechanical behavior of the material, but, successively they progress up to a crucial stage, typified by micro-crack coalition (coalescence) into macro-cracks, which finally cause specimen crumbling (Figs 5 and 6).

Table 1. Mechanical properties of sandstone measured in the longitudinal direction of loading (CL).

Specimen	*Elastic modulus*	*Compressive strength*	*Strain at compressive strength*	*Strain at failure*
	(N/mm^2)	(N/mm^2)	*(mm/mm)*	*(mm/mm)*
CL01	4565	143.6	0.03905	0.05068
CL02	4682	135.5	0.03118	0.03268
CL03	4456	141.9	0.04200	0.04660
CL05	4405	133.4	0.03720	0.04156
CL06	4328	130.6	0.03974	0.04532
CL07	3461	109.0	0.04145	0.04692
CL08	4586	151.8	0.04854	0.05214
CL10	4578	137.3	0.04468	0.04468
minimum	3461	109.0	0.03118	0.03268
maximum	4682	151.8	0.04854	0.05214
mean	4383	135.4	0.04048	0.04507
RMSE	364	11.8	0.00482	0.00563

Table 2. Mechanical properties of sandstone measured in the tangential direction of loading (CT).

Specimen	*Elastic modulus*	*Compressive strength*	*Strain at compressive strength*	*Strain at failure*
	(N/mm^2)	(N/mm^2)	*(mm/mm)*	*(mm/mm)*
CT01	4322	103.6	0.02553	0.02677
CT02	3413	130.9	0.03802	0.04166
CT05	4126	128.9	0.03502	0.04290
CT06	3604	148.7	0.04313	0.04702
CT08	3909	116.2	0.03552	0.04009
CT09	3190	137.1	0.03940	0.04516
CT10	3797	147.7	0.04757	0.05362
minimum	3190	103.6	0.02553	0.02677
maximum	4322	148.7	0.04757	0.05362
mean	3766	130.4	0.03774	0.04246
RMSE	367	15.1	0.00644	0.00761

Numerical results and their discussion

The numerical results obtained in the uniaxial compression loading are here presented and discussed.
In order to appraise the global response obtained by the numerical approach, in the following figures, color-map values of significant tensor components of damage, displacement, strain and stress, on the cubic mesh specimen, are plotted both for the longitudinal direction and for the tangential direction of loading. By preliminary examining the damage tensor components an initiate status of damage can be established. This status signs the transition from the elastic behavior to the inelastic one. Generally, inelasticity can consist of: damage or plasticity or both, as a consequence of the damage and plastic material parameters. In the present work damage and plasticity parameters are equalized and this implies the simultaneity of damage and plasticity. The damage tensor component D_{33} at the time step when damage initiate is represented in Fig. 7. In a same manner, the damage tensor component D_{11} in Fig. 8 and the damage tensor component D_{13} in Fig. 9 are plotted. From these findings, we can consider that the material maintains an elastic behavior both along the compressive loading direction D_{33} and the orthogonal loading direction D_{11}, until the sample reaches the rupture. On the contrary, the material unfavorably undergoes a very premature starting of damage along the tangential component, D_{13}.

Table 3. Mechanical properties assumed for sandstone in the numerical tests.

Property	C_{11}	C_{12} (1)	C_{13} (1)	C_{12} (1)	C_{22}	C_{23} (1)	C_{31} (1)	C_{32} (1)	C_{33}
Elastic modulus (N/mm2)	4322	2120	2051	2040	4322	2118	2051	2118	4682
		ν_{12}	ν_{13}	ν_{12}		ν_{23}	ν_{31}	ν_{32}	
Poisson's ratio (Gercek, 2007)		0.09	0.10	(2)		0.10	(2)	(2)	

(1) The mixed tensor components i≠j, according to Lekhnitskii (1963), are assumed as:

$$C_{ij} = \frac{C_{ii} \cdot C_{jj}}{C_{ii} \cdot (1+\upsilon_{ij}) + C_{jj} \cdot (1+\upsilon_{ji})} .$$

(2) The Poisson's ratios are taken as constant and, to satisfy the symmetry of the elasticity tensor, obeying the relations (Jones and Ashby, 2018):

$$\frac{\upsilon_{ij}}{C_{ii}} = \frac{\upsilon_{ji}}{C_{jj}} \text{, i, j = 1, 2, 3.}$$

Table 4. Strength properties assumed for sandstone in the numerical tests.

Tensile strength (N/mm²)								
Y^t_{11}	Y^t_{12} (1)	Y^t_{13} (1)	Y^t_{21} (1)	Y^t_{22}	Y^t_{23} (1)	Y^t_{31}	Y^t_{32} (1)	Y^t_{33}
10.4	5.1	5.4	4.9	10.4	5.5	5.4	5.5	13.5
Strain at tensile strength (mm/mm)								
E^t_{11}	E^t_{12} (1)	E^t_{13} (1)	E^t_{21} (1)	E^t_{22}	E^t_{23} (1)	E^t_{31}	E^t_{32} (1)	E^t_{33}
0.00255	0.00125	0.00128	0.00121	0.00255	0.00132	0.00128	0.00132	0.00312
Strain at tensile failure (mm/mm)								
R^t_{11}	R^t_{12} (1)	R^t_{13} (1)	R^t_{21} (1)	R^t_{22}	R^t_{23} (1)	R^t_{31}	R^t_{32} (1)	R^t_{33}
0.00268	0.00131	0.00134	0.00126	0.00268	0.00138	0.00134	0.00138	0.00327
Compressive strength (N/mm2) [6]								
Y^c_{11}	Y^c_{12} (1)	Y^c_{13} (1)	Y^c_{21} (1)	Y^c_{22}	Y^c_{23} (1)	Y^c_{31}	Y^c_{32} (1)	Y^c_{33}
103.6	50.8	53.6	48.9	103.6	55.1	53.6	55.1	135.5
Strain at compressive strength (mm/mm)								
E^c_{11}	E^c_{12} (1)	E^c_{13} (1)	E^c_{21} (1)	E^c_{22}	E^c_{23} (1)	E^c_{31}	E^c_{32} (1)	E^c_{33}
0.02553	0.01253	0.01281	0.01205	0.02553	0.01320	0.01281	0.01320	0.03118
Strain at compressive failure (mm/mm)								
R^c_{11}	R^c_{12} (1)	R^c_{13} (1)	R^c_{21} (1)	R^c_{22}	R^c_{23} (1)	R^c_{31}	R^c_{32} (1)	R^c_{33}
0.02677	0.01313	0.01343	0.01264	0.02677	0.01384	0.01343	0.01384	0.03268

The mixed tensor components: Y^t_{ij}, E^t_{ij}, R^t_{ij} and Y^c_{ji}, E^c_{ji}, R^c_{ji} for i≠j are obtained by assuming an elastic moduli-like form (Lekhnitskii, 1963) as in Table 3.

From the numerical findings, another important judgment on the overall mechanical behavior of the investigated material can be obtained by observing in Fig. 10 the color-map of the global displacement along the loading direction z. Contextually, the deformed shape at ultimate rupture is represented and the undeformed mesh is together overlapped. Here it is evident a diffuse rupture through the body mesh (as in Fig. 5 for a real specimen).

In the following Figs 11, 12 and 13, some significant strain tensor components and corresponding stress components, at the same time step 0.70, at which the post-elastic path goes on, are showed. These visualizations show that the axial strain E_{33} (Fig. 11a) at the corresponding axial stress S_{33} (Fig. 11b), as expected for this kind of specimen configuration, by preserving a certain symmetry with respect to the axis of loading, presents a distribution quite uniform with little deviation within the body centre of the specimen mesh and wider deviation at the border of the body, where stress is much sensitive to changes in the anisotropic material properties, as effect of Poisson's contraction. Realistic concentration of strain and stress are both visible at the bottom of the mesh in correspondence of the kinematic constraints.


Figure 5. Typical failure of a cubic specimen loaded in longitudinal direction.


Figure 6. Typical failure of a cubic specimen loaded in tangential direction.

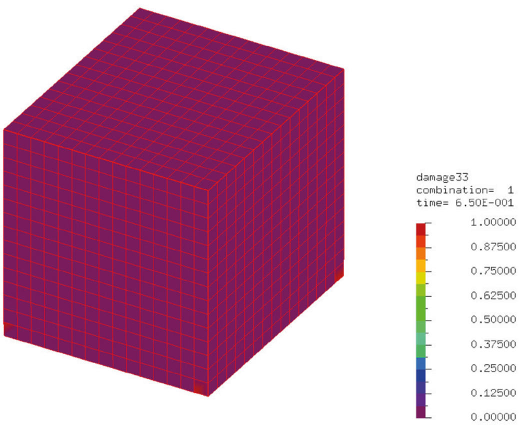

Figure 7. Color-map of the mesh displaying the initiate damage (tensor component D_{33}) for longitudinal direction of loading at time step =0.65 (at 0.5395 mm of global displacement component z)

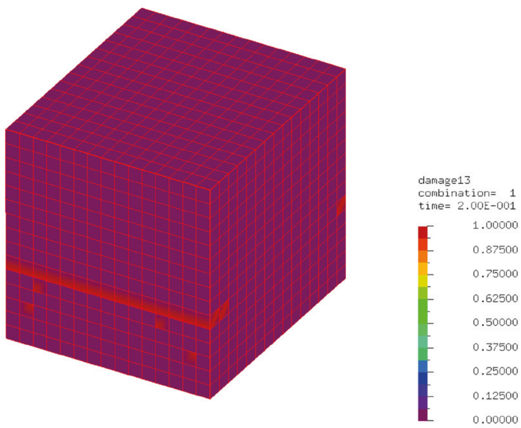

Figure 9. Color-map of the mesh displaying the initiate damage (tensor component D_{13}) for longitudinal direction of loading at time step =0.20 (at 0.1660 mm of global displacement component z).

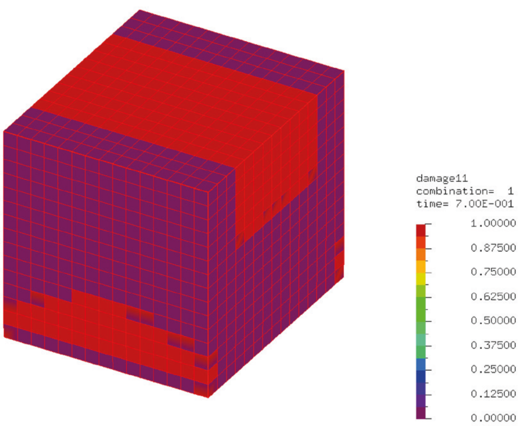

Figure 8. Color-map of the mesh displaying the initiate damage (tensor component D_{11}) for longitudinal direction of loading at time step =0.70 (at 0.5810 mm of global displacement component z).

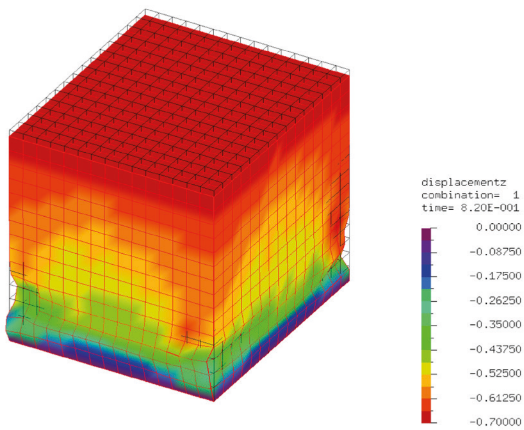

Figure 10. Color-map of the mesh displaying the global displacement component z at rupture for longitudinal direction of loading at time step =0.82 (at 0.6806 mm of global displacement component z).

In the post-elastic path, it is quite plain to distinguish among the mesh elements localization differences, as non-uniform strain distribution after damage growths, due to alternatively: strain localization at some portions and softening unloading at other portions.
In Fig. 12, the time step 0.70, in the post-elastic path, is selected for the strain E_{11} (Fig. 12a) and the corresponding stress S_{11} (Fig. 12b). These visualizations show that the transversal (respect to the loading direction) strain at the corresponding transversal stress proceeds in a quite uniformly distributed mode within the body of the specimen mesh, by preserving a certain symmetry only with respect to one transversal direction according to the transversely isotropy of the material. An effect of reduction of values, arc-shaped, is visible in the color-maps, this being a credible reduction caused by the relatively (respect to the low resistance of the material) high resistance opposed by the constrained bottom edge.
In Fig. 13, the time step 0.70, in the post-elastic path, is selected for the strain E_{13} (Fig. 13a) and the corresponding stress S_{13} (Fig. 13b). These images show that the tangential strain at the corresponding tangential stress roughly is uniformly distributed in the body mesh, also some major diagonal seems to follow the arc-shape of the transversal component before discussed. A slight concentration of strain and stress is both visible at the bottom of the mesh in correspondence of the kinematic constraints.
A similar set of figures are built, likewise for the longitudinal direction of loading above discussed, for the tangential direction of loading.
Figs 14, 15 and 16 display the damage initiate at a certain time step for significant damage tensor components: D_{33} (Fig. 14), D_{11} (Fig. 15) and D_{13} (Fig. 16) for tangential direction of loading. By observing these figures it is plain that the material remains elastic

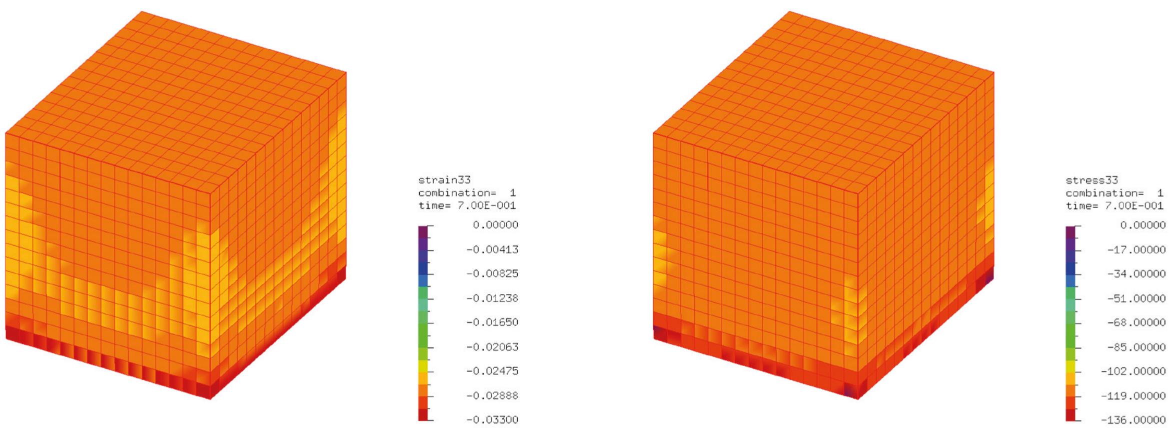

Figure 11. Color-map of the mesh displaying the strain tensor component E_{33} (a) and the correspondent stress tensor component S_{33} (b) for longitudinal direction of loading at time step =0.70.

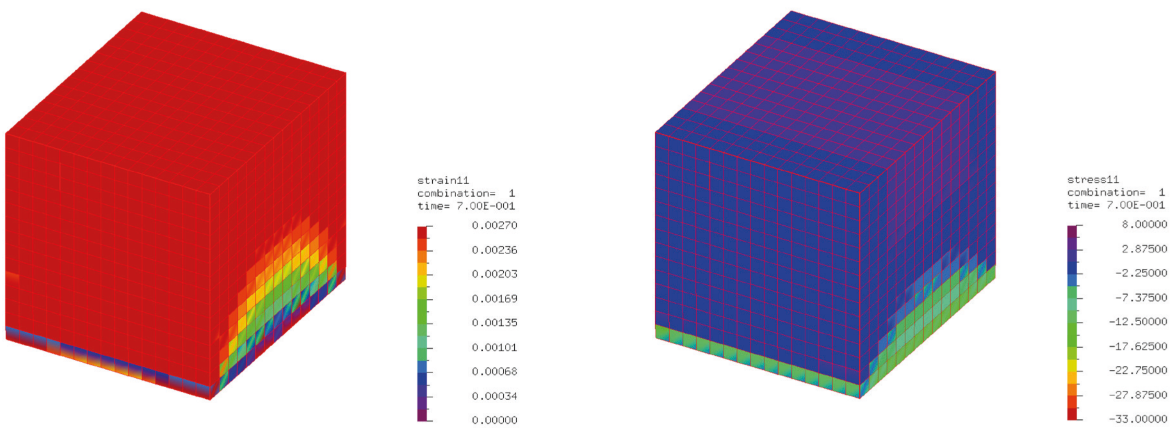

Figure 12. Color-map of the mesh displaying the strain tensor component E_{11} (a) and the correspondent stress tensor component S_{11} (b) for longitudinal direction of loading at time step =0.70.

for the component along the loading axis direction, D_{33}, and for the component in the direction orthogonal to loading, D_{11}, until it reaches the rupture, on the contrary the material undergoes an unfavorable premature start of damage along the tangential component D_{13}.
In Fig. 17 the global displacement along the loading direction z is color-mapped. Here the deformed shape at ultimate rupture is represented and overlapped with the undeformed mesh. Some elements appear to form slice formations at rupture in the vertical plane (as in Fig. 6 for a real specimen).
In the following Figs 18, 19 and 20, significant strain tensor components together with the corresponding stress ones, at a time step 0.65 , in the post-elastic path, are color-mapped. These visualizations show that the axial strain E_{33} (Fig. 18a) at the corresponding axial stress S_{33} (Fig. 18b) proceeds as quite uniformly distributed within the body of the specimen mesh, by preserving a certain symmetry with respect to the axis of loading. Realistic concentration of strain and stress are both visible at the bottom of the mesh in correspondence of the kinematic constraints.
In Fig. 19, the color-maps at the selected time step 0.70 in the post-elastic path are represented for the strain E_{11} (Fig. 19a) and the corresponding stress S_{11} (Fig. 19b). These visualizations show that in the post-elastic path strain and related stress show a plain clustering into vertical slices of the mesh elements.
In Fig. 20 the time step 0.70, in the post-elastic path, is selected for the strain E_{13} (Fig. 20a) and the corresponding stress S_{13} (Fig. 20b). It is evident that in the post-elastic path in strain and relative stress clustered concentrations prevail in the mesh body. This is a clear signal of an imminent, chaotic and diffuse disintegration of the inner structure of the material.
Overall, the numerical results have permitted to contextually observe in the investigated stone material,

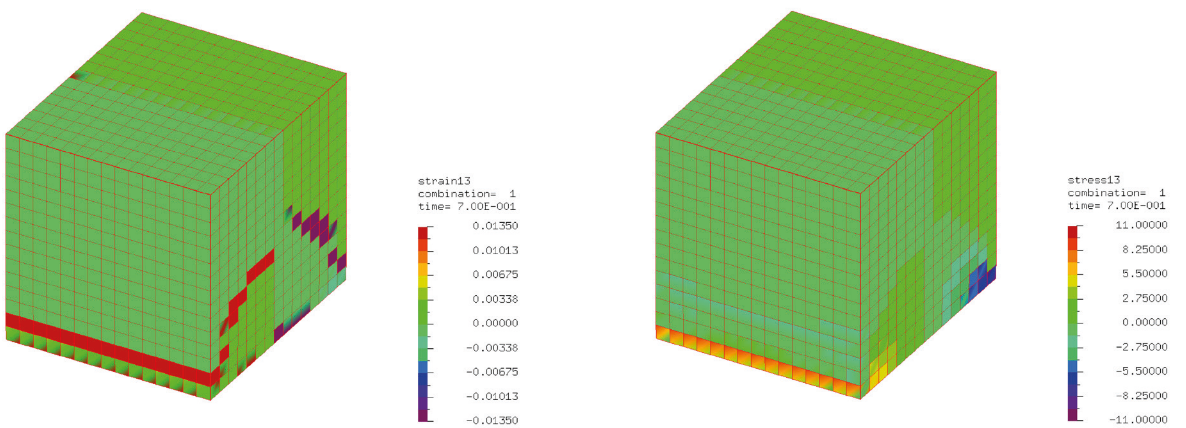

Figure 13. Color-map of the mesh displaying the strain tensor component E_{13} (a) and the correspondent stress tensor component E_{13} (b) for longitudinal direction of loading at time step =0.70.

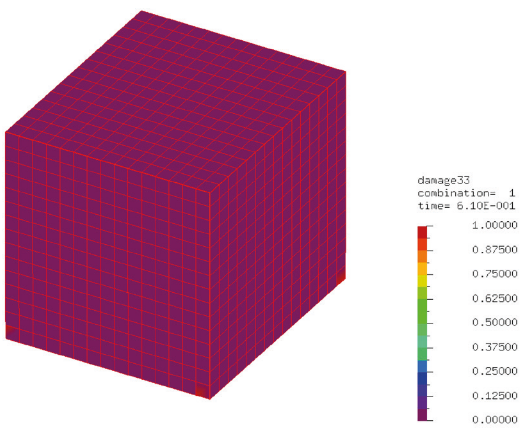

Figure 14. Color-map of the mesh displaying the initiate damage (tensor component D_{33}) for tangential direction of loading at time step =0.61 (at 0.4575 mm of global displacement component z).

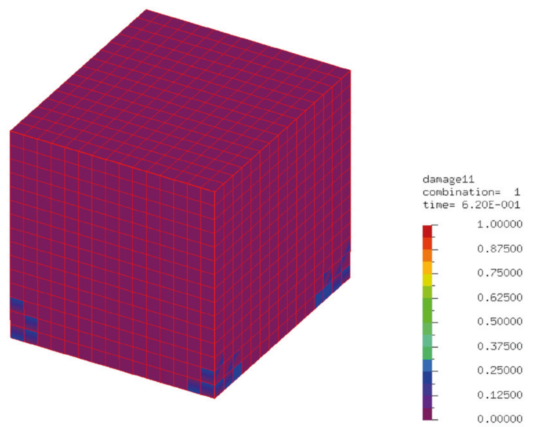

Figure 15. Color-map of the mesh displaying the initiate damage (tensor component D_{11}) for tangential direction of loading at time step =0.62 (at 0.4650 mm of global displacement component z).

under loading, both softening and localization of strain. When the stone material entirely reaches the compressive strength, a coexisting contrast in behavior of some mesh elements can be viewed: a lot of them show localization of strain and others evidence softening of strain. So, damage can be due to both compressive and tensile stresses.

Verification of the numerical model

The validity of the elastic-plastic-damage numerical model is based on the comparison of the FEM numerical analyzes with the experimental tests of the sandstone.

The mesh dependency is a part considered by incrementing the number of mesh elements. At this concern, as expected for the Finite Element Method, a monotonically convergence of the numerical solution is obtained.

Concerning the numerical issue of the mesh dependency on damage, the model turned out to be not excessively sensitive, so no particular strategy is adopted.

Stress-strain response - In Fig. 21, the experimental couple of stress-strain points, data-logged in a test (specimen CL02) along the longitudinal direction of loading, are plotted. Correspondingly, in the same stress-strain diagram of Fig. 21, contextually, for comparison purpose, the numerical values of strain and stress are overlapped. These values are the overall average at the integration points on the upper face of the mesh model. Both the experimental and numerical values of the above diagram are referred to the same uniaxial compression loading on a specimen having the same nominal geometrical dimensions. We can see in Fig. 21 that the numerical diagram quite agree with the experimental one.

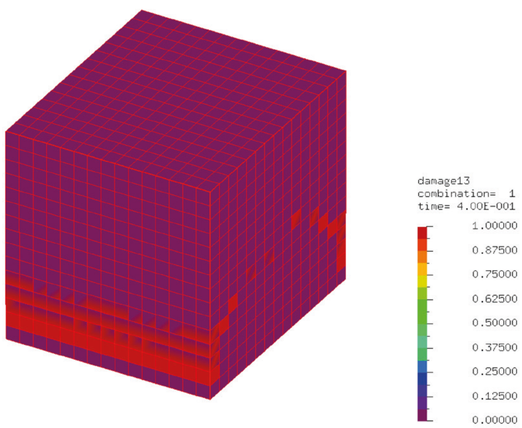

Figure 16. Color-map of the mesh displaying the initiate damage (tensor component D_{13}) for tangential direction of loading at time step =0.40 (at 0.3000 mm of global displacement component z).

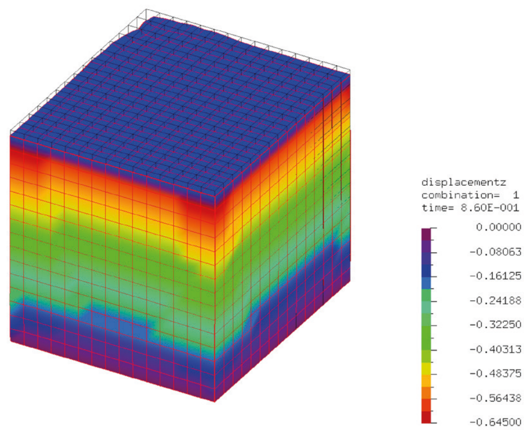

Figure 17. Color-map of the mesh displaying the global displacement component z at rupture for tangential direction of loading at time step =0.86 (at 0.6450 mm of global displacement component z).

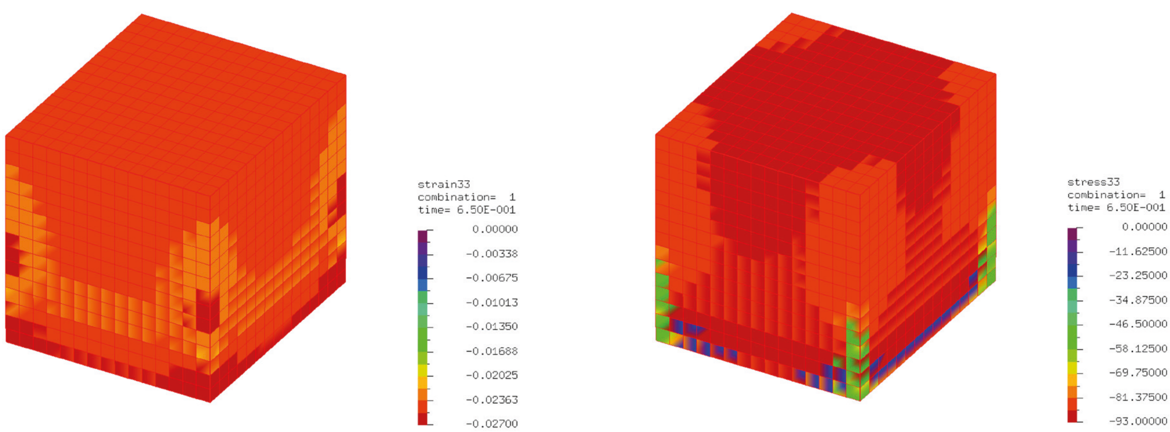

Figure 18. Color-map of the mesh displaying the strain tensor component E_{33} (a) and the correspondent stress tensor component S_{33} (b) for tangential direction of loading at time step =0.65.

In Fig. 22, the diagram of stress-strain of the couple of experimental points data-logged in the mechanical compression test (specimen CT01) along the tangential direction of loading are plotted. The numerical stress-strain points, also, for a same mesh model of specimen and loading condition, are overlapped for comparison purpose. We can see in Fig. 22 that the numerical diagram quite agree with the experimental one.

General discussion

On the whole, the experimental data on the stone specimens under uniaxial compression loading have revealed that the stress-strain path is quite alike to those of sandstones reported in scientific literature. We can notice that after the first downward flexing, due to crack closure, a defined elastic-linear path is well distinguishable. Subsequently, at the post-peak, the material experiences a quite short softening, followed by a brittle failure. These features can be detected, for the investigated material, both in the longitudinal direction and in the tangential direction of loading (Figs 21 and 22).

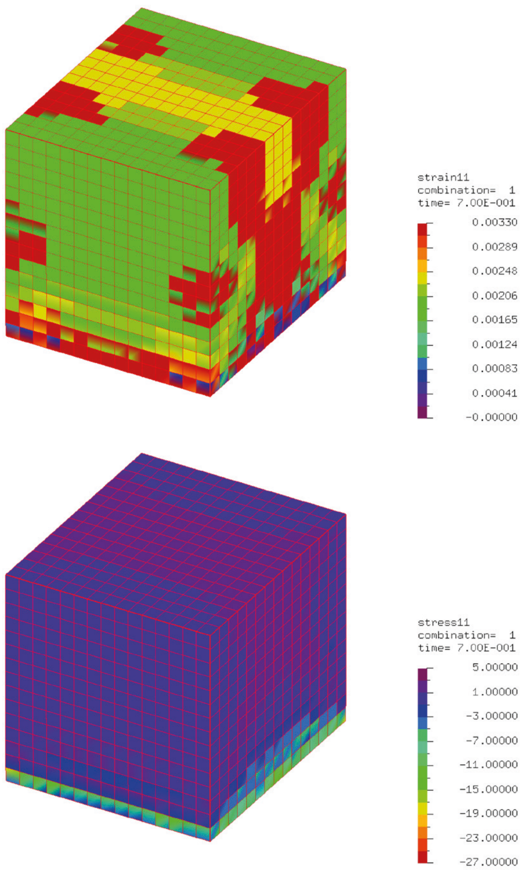

Figure 19. Color-map of the mesh displaying the strain tensor component E_{11} (a) and the correspondent stress tensor component S_{11} (b) for tangential direction of loading at time step =0.70.

The graphing of numerical stress-strain diagrams of the material model, until failure occurs, is compared with that of the experimental test to check the validity of the proposed model. This comparison has highlighted that the numerical predictions of the stress-strain path along the elastic and inelastic phase, plastic and damage, rather agree with the experimental values.

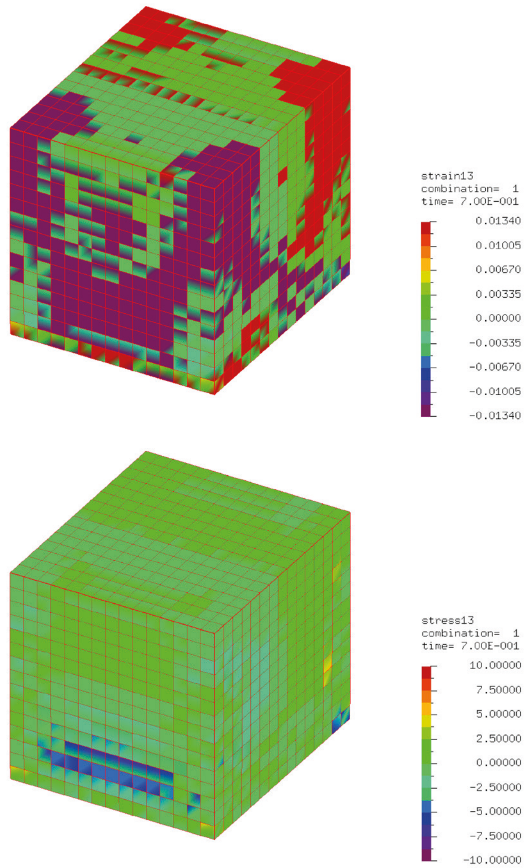

Figure 20. Color-map of the mesh displaying the strain tensor component E_{13} (a) and the correspondent stress tensor component S_{13} (b) for tangential direction of loading at time step =0.70.

The overall results have shown that the proposed model can usefully outline the material behavior, both elastic and post-peak, and failure modes of the stone material.

Some weakness of the investigated material is displayed by the numerical results such as the premature damage in the tangential plane of the material that is a remarkable unfavorable issue for building material in a seismic event, by implying seismic vulnerability.

Conclusions

This work deals with a FEM mechanical characterization of sandstone as building material in masonry constructions. The behavior of the stone material under compression can be recognized like quasi-brittle material. To represent the damage effects a diversification, in the yield functions, between each tensor components is usefully introduced in the numerical model. The advised numerical constitutive model is implemented within a general-purpose Finite Element Method framework, coded in a specific software in another work (De Luca, 2022). This model is applied to numerically reproduce the stone stress-strain path until failure, under uniaxial compression loading. Uniaxial compression tests, by means of a servo-controlled press machine, and their related configuration and loading conditions, here illustrated, are employed to validate the numerical predictions, carried out for the same mesh model of specimen.

On the basis of the experimental data, stress-strain diagrams are plotted whose analysis has delivered the deformation behavior and the strength characteristics of the sandstone material. In the experimental tests a typical failure of localization deformation is observed in the material.

The obtained numerical results have shown, by comparison, to be quite concord with the experimental ones. Also, the same model is capable to give indicative signal of the failure mechanisms involved in the stone material when the compression strength is completely mobilized under loading.

The proposed model, through its fully anisotropic constitutive representation of plastic and damage coupling, can effectively represent a complex behavior, which occurs in the post-elastic region of a generic stone material.

The present work can support numerical design software code in terms of reliability and completeness of representation of a more realistic behavior of a basic material in masonry of heritage buildings.

However, the present work, being based on a generic approach that is rather unrelated to the kind of loading and stone, can be employed in a future research to analyze other loading conditions and different stone materials in masonry structures.

Acknowledgements

The authors wish to thank the SAFE School of the University of Basilicata to have supplied the Laboratory of Building Materials in the experimental stage.

REFERENCES

Agelopoulou H.A., Sfakianakis M.G., Hatzigeorgiou G.D., Beskos D.E. (2005). Static and dynamic analysis of masonry buildings by a nonlinear 3-D FEM. *WIT Transactions on The Built Environment* 81.

Alejandre F.J., Flores-Ales V., Villegas R., Garcia-Heras J., Moron E. (2014). Estimation of Portland cement mortar compressive strength using microcores. *Influence of shape and size. Construction and Building Materials* 55: 359-364.

Binda L., Modena C., Baronio G., Abbaneo S. (1997). Repair and investigation techniques for stone masonry walls. *Construction and Building Materials* 11(3): 133-142.

Brandonisio G., Lucibello G., Mele E., De Luca A. (2013). Damage and performance evaluation of masonry churches in the 2009 L'Aquila earthquake. *Engineering Failure Analysis* 34: 693-714.

Chiarelli A.S., Shao J.F., Hoteit N. (2003). Modeling of elastoplastic damage behavior of a claystone. *International Journal of plasticity* 19(1): 23-45.

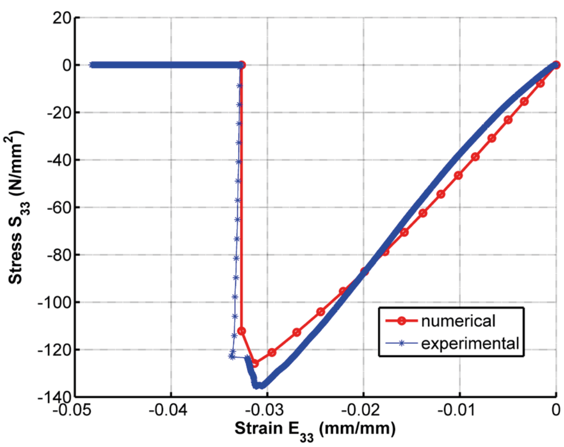

Figure 21. The stress-strain diagram, of the tensor component D_{33}, for longitudinal direction of loading, obtained from experimental data and numerical model results.

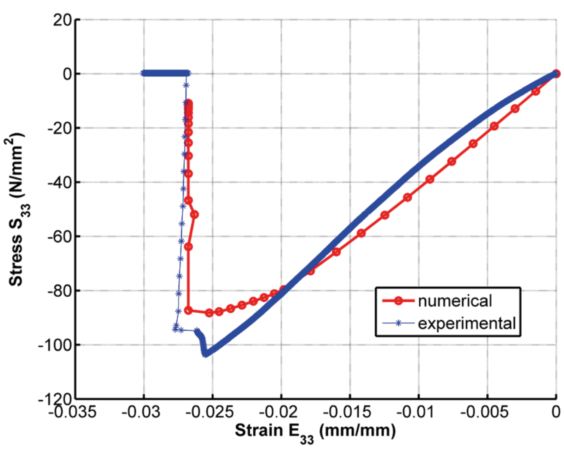

Figure 22. The stress-strain diagram, of the tensor component D_{33}, for tangential direction of loading, obtained from experimental data and numerical model results.

de Angelis F. (2012a). *Computational aspects in the elasto/viscoplastic material behavior of solids*. In: Advanced Materials Research, Vol. 567: 192-199. Bäch, Switzerland, Trans Tech Publications Ltd.

de Angelis F. (2012b). *Numerical algorithms for J2 viscoplastic models*. In: Advanced Materials Research, Vol. 567: 267-274. Bäch, Switzerland, Trans Tech Publications Ltd.

De Angelis F. (2012c). On the structural response of elasto/viscoplastic materials subject to time-dependent loadings. *Structural Durability & Health Monitoring* 8(4): 341.

de Angelis F. (2012d). *On constitutive relations in non-smooth elasto/viscoplasticity*. In: Advanced Materials Research, Vol. 566: 691-698). Bäch, Switzerland, Trans Tech Publications Ltd.

de Angelis F. (2012e). *Computational issues in rate-dependent plasticity models*. In: Advanced Materials Research, Vol. 566: 70-77). Bäch, Switzerland, Trans Tech Publications Ltd.

De Luca V., Della Chiesa A. (2013). A creep non-linear FEM analysis of glulam timber. *Mechanics of advanced materials and structures* 20(6): 489-496.

De Luca V., Marano C. (2012). Prestressed glulam timbers reinforced with steel bars. *Construction and Building Materials* 30: 206-217.

De Luca V., Sabia D. (2007). Mechanical compression tests to model timber structures behaviour. *WIT Transactions on Engineering Sciences* 57.

De Luca V., Bentivenga M., Cavalcante F., Lezzerini M., Marano C., Palladino G., Prosser G. (2019). Geological Features and Physical and Mechanical Properties of the Gorgoglione Building Stone of Basilicata (Southern Italy). *Geoheritage* 11(4): 1621-1629.

De Luca V., Bentivenga M., Palladino G., Grimaldi S., Prosser G. (2015). *A Finite Element Analysis of the Brindisi di Montagna Scalo Earthflow (Basilicata, Southern-Italy)*. In: Engineering Geology for Society and Territory, Vol. 2: 1239-1243. Cham, Springer.

De Luca V. (2022). *A large strains Finite Element Method framework for elastic-inelastic material models multi-yield driven*, unpublished paper.

Drdácký M., Slížková Z. (2008). Mechanical characteristics of historical mortars from tests on small-sample non-standard specimens. *Mater. Sci. Appl. Chem.* 17(1): 20-29.

Drdácký M., Mašín D., Mekonone M.D., Slížková Z. (2008, September). *Compression tests on non-standard historic mortar specimens*. In: HMC08-Historical Mortars Conference (Lisbon, 24-26 September 2008): 1-10. Lisbon, LNEC.

Faria R., Oliver J., Cervera M. (1998). A strain-based plastic viscous-damage model for massive concrete structures. *International journal of solids and structures* 35(14): 1533-1558.

Gao W., Chen X., Hu C., Zhou C., Cui S. (2020). New damage evolution model of rock material. *Applied Mathematical Modelling* 86: 207-224.

García D., San-José J.T., Garmendia L., Larrinaga P. (2012). Comparison between experimental values and standards on natural stone masonry mechanical properties. *Construction and Building Materials* 28(1): 444-449.

Gercek H. (2007). Poisson's ratio values for rocks. *International Journal of Rock Mechanics and Mining Sciences* 44(1): 1-13.

Grady D.E., Kipp M.E. (1979, October). *The micromechanics of impact fracture of rock*. In: International Journal of Rock Mechanics and Mining Sciences & Geomechanics Abstracts, Vol. 16, No. 5: 293-302). Great Britain, Pergamon.

Guerreiro J., Proença J.M., Ferreira J.G., Gago A.S. (2017). Bonding and anchoring of a CFRP reinforced render for the external strengthening of old masonry buildings. *Construction and Building Materials* 155: 56-64.

Hatzigeorgiou G., Beskos D., Theodorakopoulos D., Sfakianakis M. (2001). A simple concrete damage model for dynamic FEM applications. *International Journal of Computational Engineering Science* 2(02): 267-286.

Hudson J.A., Harrison J.P. (1997). *Engineering rock mechanics-An introduction to the principles*. Imperial College of Science, Technology and Medicine, University of London, Elsevier Science: 193, 195.

Indelicato F. (1993). A statistical method for the assessment of concrete strength through microcores. *Materials and Structures* 26(5): 261-267.

Indelicato F. (1998). A proposal for the prediction of the characteristic ube strength of concrete from tests on small cores of various diameters. *Materials and Structures* 31(4): 242-246.

Ivorra S., Pallarés F.J., Adam J.M. (2009). Experimental and numerical results from the seismic study of a masonry bell tower. *Advances in Structural Engineering* 12(2): 287-293.

Jones D.R., Ashby M.F. (2018). *Engineering materials 1: An introduction to properties, applications and design*. Oxford, United Kingdom, Butterworth-Heinemann.

Kaur G., de Oliveira Frascá M.H.B., Pereira D. (2021). Natural Stones: architectonic heritage and its global relevance. *Episodes Journal of International Geoscience* 44(1): 1-2.

Krajcinovic D., Silva M.A.G. (1982). Statistical aspects of the continuous damage theory. *International Journal of Solids and Structures* 18(7): 551-562.

Lekhnitskii S.G. (1963). *Theory of an anisotropic elastic body*. Translation by P. Fern. San Francisco, Brandstatter ed., Holden-Day Inc.

Lourenço P.B. (2006). Recommendations for restoration of ancient buildings and the survival of a masonry chimney. *Construction and Building Materials* 20(4): 239-251.

Lucibello G., Brandonisio G., Mele E., De Luca A. (2013). Seismic damage and performance of Palazzo Centi after L'Aquila earthquake: A paradigmatic case study of effectiveness of mechanical steel ties. *Engineering Failure Analysis* 34: 407-430.

Mazars J. (1986). A description of micro-and macroscale damage of concrete structures. *Engineering Fracture Mechanics* 25(5-6): 729-737.

Molladavoodi H., Mortazavi A. (2011). A damage-based numerical analysis of brittle rocks failure mechanism. *Finite Elements in Analysis and Design* 47(9): 991-1003.

Mosele F., Barbieri L., Botti F. (2016, November). *Reconstruction of a rural building damaged by 2012 Emilia earthquake using tall reinforced masonry walls designed accounting for p-Δ effects*. In: Brick and Block Masonry. Proceedings of the 16th International Brick and Block Masonry Conference (Padova, 26-30 June 2016), ed. by C. Modena, F. da Porto, M.R. Valluzz. Boca Raton - London - New York - Leiden, CRC Press.

Pereir D., Marker B. (2016). The value of original natural stone in the context of architectural heritage. *Geosciences* 6(1): 13.

Ramalho M.A., Taliercio A., Anzani A., Binda L., Papa E. (2008). A numerical model for the description of the nonlinear behaviour of multi-leaf masonry walls. *Advances in Engineering Software* 39(4): 249-257.

Ramos L.F., Lourenço P.B. (2004). Modeling and vulnerability of historical city centers in seismic areas: a case study in Lisbon. *Engineering structures* 26(9): 1295-1310.

Romera L.E., Hernández S., Gutierrez R. (2008b). Numerical characterization of the structural behaviour of the Basilica of Pilar in Zaragoza (Spain). Part 2: Constructive process effects. *Advances in Engineering Software* 39(4): 315-326.

Romera L.E., Hernández S., Reinosa J.M. (2008a). Numerical characterization of the structural behaviour of the Basilica of Pilar in Zaragoza (Spain). Part 1: Global and local models. *Advances in Engineering Software* 39(4): 301-314.

Sandbhor S., Botre R. (2013). A systematic approach towards restoration of heritage buildings-a case study. International *Journal of Research in Engineering and Technology* 2(3): 229-238.

Šekularac N., Debljović Ristić N., Mijović D., Cvetković V., Barišić S., Ivanović-Šekularac J. (2019). The use of natural stone as an authentic building material for the restoration of historic buildings in order to test sustainable refurbishment: Case study. *Sustainability* 11(15): 4009.

Selli R. (1962). Il Paleogene nel quadro della geologia dell'Italia meridionale. *Memorie Società Geologica Italiana* 3: 737-790.

Senthivel R., Lourenço P.B. (2009). Finite element modelling of deformation characteristics of historical stone masonry shear walls. *Engineering structures* 31(9): 1930-1943.

Shao J.F., Chau K.T., Feng X.T. (2006). Modeling of anisotropic damage and creep deformation in brittle rocks. International *Journal of Rock Mechanics and Mining Sciences* 43(4): 582-592.

Skłodowski M. (2006). *Micro-cores technology for testing of historical materials*. In: J. Radic, V. Rajcic, R. Zarnic (eds), *Proc. Int. Conf. Heritages Protection-construction aspects*: 205-211. Dubrovnik.

Triantafillou T.C., Fardis M.N. (1997). Strengthening of historic masonry structures with composite materials. *Materials and Structures* 30(8): 486-496.

Tuncan M., Arioz O., Ramyar K., Karasu B. (2008). Assessing concrete strength by means of small diameter cores. *Construction and Building Materials* 22(5): 981-988.

Varas-Muriel M.J., Pérez-Monserrat E.M., Vázquez-Calvo C., Fort R. (2015). Effect of conservation treatments on heritage stone. Characterisation of decay processes in a case study. *Construction and Building Materials* 95: 611-622.

Vasanelli E., Calia A., Colangiuli D., Micelli F., Aiello M.A. (2016). Assessing the reliability of non-destructive and moderately invasive techniques for the evaluation of uniaxial compressive strength of stone masonry units. *Construction and Building Materials* 124: 575-581.

Vasanelli E., Colangiuli D., Calia A., Sbartaï Z.M., Breysse D. (2017). Combining non-invasive techniques for reliable prediction of soft stone strength in historic masonries. *Construction and Building Materials* 146: 744-754.

Wu J.Y., Li J., Faria R. (2006). An energy release rate-based plastic-damage model for concrete. *International journal of Solids and Structures* 43(3-4): 583-612.

Xie S., Han Z., Lin H. (2022). A quantitative model considering crack closure effect of rocks. *International Journal of Solids and Structures* 111758.

Yavartanoo F., Kang T.H.K. (2022). Retrofitting of unreinforced masonry structures and considerations for heritage-sensitive constructions. *Journal of Building Engineering* 49: 103993.

Yazdani S., Schreyer H.L. (1988). An anisotropic damage model with dilatation for concrete. *Mechanics of Materials* 7(3): 231-244.

(ms. pres. 28 giugno 2022; ult. bozze 12 dicembre 2022)